



Science Arts & Métiers (SAM)

is an open access repository that collects the work of Arts et Métiers Institute of Technology researchers and makes it freely available over the web where possible.

This is an author-deposited version published in: <https://sam.ensam.eu>
Handle ID: <http://hdl.handle.net/10985/17843>

To cite this version :

Mathieu SPECKLIN, Michael DELIGANT, Sofiane KHELLADI - A naturally anti-diffusive compressible two phases Kapila model with boundedness preservation coupled to a high order finite volume solver - Computers & Fluids - Vol. 114, p.265-273 - 2015

Any correspondence concerning this service should be sent to the repository

Administrator : scienceouverte@ensam.eu



A naturally anti-diffusive compressible two phases Kapila model with boundedness preservation coupled to a high order finite volume solver

M. Deligant ^{a,*}, M. Specklin ^{a,b}, S. Khelladi ^a

^a DynFluid Lab., Arts et Métiers ParisTech, 151 boulevard de l'Hôpital, 75013 Paris, France

^b School of Mechanical and Manufacturing Engineering, Dublin City University, Glasnevin, Dublin, Ireland

A B S T R A C T

This paper presents a two phases flow model combined with a high order finite volume solver on unstructured mesh. The solver is highly conservative and preserves the sharpness of the interface without any reconstruction. Special care has been taken for boundedness preservation, as a high order scheme does not guaranty the boundedness of the volume fraction.

The efficiency of the method is demonstrated with two numerical experiments: the simple advection test and the interaction between the shock and a bubble. Although experiments have been carried out with fine mesh, it is also demonstrated that the method allows satisfactory results to be obtained with coarse mesh.

1. Introduction

Multiphase flows intervene in a wide range of industrial problems, including aerospace, atmospheric, biological, chemical, civil, mechanical, and nuclear systems. Currently, these type of flows are not mastered and form the topic of much challenging research.

We discuss in this study the methods of the resolved surface type for two immiscible fluids. This family of methods is able to capture coherent interfaces, in contrary to dispersed multi-phase flow methods. A widely used resolved surface approach is the volume of fluid (VOF) method [1], where a marker is transported. This marker, defined as the volume fraction (between 0 and 1) represents each fluid's parts in the control volumes. For the VOF method, the conservation feature is not hard to obtain. However, the main weakness of this kind of method is the numerical diffusion and the interface smoothing, especially for low order schemes. To avoid these problems, several methods of interface reconstruction have been proposed. These algorithms are nevertheless usually implemented for cartesian or structured meshes (SLIC Noh and Woodward [2], PLIC Youngs [3]) and with a first order accuracy. Heavier and more sophisticated methods have been proposed with a second order accuracy [4], still with cartesian meshes. Another possibility to avoid smoothing problems lies in the interface sharpening, for example by adding a compressive term as a source term

in the fluid governing equations [5]. Finally, models avoiding explicit geometrical reconstruction have been proposed, as for example the CICSAM method [6] or the approach developed by Chen et al. [7], where the numerical diffusion is reduced thanks to a combination of high order accurate schemes near the interface. Local mesh refinement could also handle low diffusion [8].

Another type of resolved surface approaches are the front tracking methods, represented by the level set method [9]. The latter method is based on the transport of a distance function. Because of the smooth property of this function, the level set method is very slightly diffusive. On the other hand, the mass conservation is difficult to obtain with such a method for complex flows. To obtain the benefits of both types of resolved surface approach, coupled level set and VOF methods have already been developed, for structured meshes [10], and for unstructured ones [11,12].

Different models are available in the literature for multiphase flow, for instance: the Baer–Nunziato model [13], the Kapila model [14] and the Saurel–Abgrall model [15]. While, some of them have 7 equations [16], other reduce to 6 [17] or even 5 equations [18]. In this paper, a two-phase Kapila model is proposed based on a high order finite volume solver using moving least square reconstruction (MLS) [19]. The MLS approach allows a high spatial order of accuracy to be obtained for the variables. In this case, the complex methods of interface reconstruction are no more necessary to reduce the diffusion of the step variables, like the volume fraction. However, when this marker is transported with high order schemes, the problem of boundedness appears. A wide analysis of the different

* Corresponding author.

E-mail address: michael.deligant@ensam.eu (M. Deligant).

solutions to circumvent this problem has been made by Waterson et al. [20]. The TVD (total variation diminishing) schemes are typically employed as boundedness criteria. Nevertheless, they tend to more or less smear the interface for interfacial flows [21]. Another frequently-used approach is the NVD (normalized variable diagram) non-linear approach, which is based on a switch between different differencing schemes for the Riemann problem, depending on the flow direction and velocity [22]. This solution has the drawback of being heavy to implement. In this study, a simple algorithm with the same global effect is used, reducing the spatial order if the variable is exceeding the bounds. Finally, the main advantage of the proposed MLS approach lies in its applicability to coarse and unstructured meshes.

In Section 2, the moving least squares approach for a finite volume solver (FV-MLS) is presented. The Kapila model introduced in Section 3 is used to solve the Euler equations for a compressible two-phase flow. Section 4 presents the algorithm used to preserve the boundedness. Our model is validated with two test cases, of which set-up and results are discussed in Section 5. Finally, Section 6 summarizes and concludes the current formulation.

2. Finite volume moving-least-squares method

2.1. Higher-order finite volume method

The main idea behind the higher-order formulation of the FVM is the use of reconstructed variables of a given order of accuracy, into the numerical flux, to achieve the desired order of the scheme. In other terms, the FVM solver will deal with average values of the field variables, and the solution is assumed constant within each control volume. So, the underlying spatial representation would be that of a piecewise constant flow field. High order schemes are constructed by substituting the constant representation by a piecewise continuous reconstruction of the flow variables inside each cell. The estimation of the numerical flux, regardless of their order without reconstruction, using the piecewise continuous reconstruction will ensure the sought order.

In order to improve the order of accuracy, we will compute the flux functional at the cell interfaces, rather than the use of centroid values, and we will use a higher-order reconstruction of \mathbf{U} at the interfaces.

2.1.1. Higher-order reconstruction procedure

The Taylor expansion of \mathbf{U} at the vicinity of (I), where (I) makes reference to the centroid cell, is given by:

$$\mathbf{U}(\mathbf{x})|_I = \mathbf{U}_I + \sum_{\alpha=1}^N \sum_{\beta=0}^{\alpha} \frac{1}{\beta! (\alpha - \beta)!} (x - x_I)^{\alpha - \beta} (y - y_I)^{\beta} \frac{\partial^{\alpha} \mathbf{U}_I}{\partial x^{\alpha - \beta} \partial y^{\beta}} + o(N) \quad (1)$$

N being the order of accuracy of the expansion.

The main difficulty of evaluating $\mathbf{U}(\mathbf{x})|_I$ is the estimation of higher order derivatives. The FV-MLS method overcomes this difficulty by using Moving Least Squares Approximations. This approach is somewhat different than the usual approach of high-order finite volume schemes. The usual approach is pragmatic and *bottom-up*. Starting from an underlying piecewise constant representation, a discontinuous reconstruction of the field variables is performed at the cell level. The FV-MLS method starts from a high-order and highly regular representation of the solution, obtained by means of Moving Least-Squares approximation [23], and well suited for general, unstructured grids. This approach is directly suitable for the discretization of elliptic/parabolic equations and high order spatial terms [24]. For equations with a predominantly hyperbolic character, the global representation is *broken* locally, at

the cell level, into a piecewise polynomial reconstruction, which allows to use the powerful finite volume technology of Godunov-type schemes for hyperbolic problems (e.g. Riemann solvers, limiters) [24].

2.2. Moving least squares reproducing kernel approximations

2.2.1. General formulation

The Moving Least Squares approximations [23] is a very usual technique in the meshless community. It is very well suited for the approximation of scattered data. In this section we introduce briefly this technique. We refer the reader to [23,25,26,24] and references therein. Let us consider a function $U(\mathbf{x})$ defined in a domain Ω , the basic idea of the MLS approach is to approximate $U(\mathbf{x})$, at a given point \mathbf{x} , through a weighted least-squares fitting of $U(\mathbf{x})$ in a neighborhood of \mathbf{x} as

$$U(\mathbf{x}) \approx \hat{U}(\mathbf{x}) = \sum_{i=1}^m p_i(\mathbf{x}) \alpha_i(\mathbf{z}) \Big|_{\mathbf{z}=\mathbf{x}} = \mathbf{p}^T(\mathbf{x}) \boldsymbol{\alpha}(\mathbf{z}) \Big|_{\mathbf{z}=\mathbf{x}} \quad (2)$$

$\mathbf{p}^T(\mathbf{x})$ is an m -dimensional polynomial basis and $\boldsymbol{\alpha}(\mathbf{z})|_{\mathbf{z}=\mathbf{x}}$ is a set of parameters to be determined, such that they minimize the following error functional:

$$J(\boldsymbol{\alpha}(\mathbf{z})|_{\mathbf{z}=\mathbf{x}}) = \int_{\mathbf{y} \in \Omega_{\mathbf{x}}} W(\mathbf{z} - \mathbf{y}, h) \Big|_{\mathbf{z}=\mathbf{x}} \left[U(\mathbf{y}) - \mathbf{p}^T(\mathbf{y}) \boldsymbol{\alpha}(\mathbf{z}) \Big|_{\mathbf{z}=\mathbf{x}} \right]^2 d\Omega_{\mathbf{x}} \quad (3)$$

being $W(\mathbf{z} - \mathbf{y}, h)|_{\mathbf{z}=\mathbf{x}}$ a *kernel* with compact support (denoted by $\Omega_{\mathbf{x}}$) centered at $\mathbf{z} = \mathbf{x}$. The parameter h is the smoothing length, which is a measure of the size of the support $\Omega_{\mathbf{x}}$. For example, a polynomial cubic basis is given by:

$$\mathbf{p}(\mathbf{x}) = (1 \ x \ y \ xy \ x^2 \ y^2 \ x^2y \ xy^2 \ x^3 \ y^3)^T \quad (4)$$

which provides cubic completeness. In the above expression, (x, y) denotes the Cartesian coordinates of \mathbf{x} . In order to improve the conditioning, the polynomial basis is locally defined and scaled: if the shape functions are going to be evaluated at \mathbf{x}_I , the polynomial basis is evaluated at $(\mathbf{x} - \mathbf{x}_I)/h$. Following [26,24], the interpolation structure can be identified as

$$\begin{aligned} \hat{U}(\mathbf{x}) &= \mathbf{p}^T \left(\frac{\mathbf{x} - \mathbf{x}_I}{h} \right) \mathbf{M}^{-1}(\mathbf{x}) \mathbf{P}_{\Omega_{\mathbf{x}}} \mathbf{W}(\mathbf{x}) \mathbf{U}_{\Omega_{\mathbf{x}}} = \mathbf{N}^T(\mathbf{x}) \mathbf{U}_{\Omega_{\mathbf{x}}} \\ &= \sum_{j=1}^{n_{\mathbf{x}}} N_j(\mathbf{x}) U_j \end{aligned} \quad (5)$$

where we define the moment matrix \mathbf{M} as (see [24]):

$$\mathbf{M} = \mathbf{P}_{\Omega_{\mathbf{x}}} \mathbf{W}(\mathbf{x}) \mathbf{P}_{\Omega_{\mathbf{x}}}^T \quad (6)$$

and the matrices $\mathbf{P}_{\Omega_{\mathbf{x}}}$ and $\mathbf{U}_{\Omega_{\mathbf{x}}}$ reads as follows:

$$\mathbf{P}_{\Omega_{\mathbf{x}}} = (\mathbf{p}(\mathbf{x})_1 \cdots \mathbf{p}(\mathbf{x})_{n_{\mathbf{x}}}) \quad (7)$$

$$\mathbf{U}_{\Omega_{\mathbf{x}}} = (U_{x_1} \cdots U_{x_{n_{\mathbf{x}}}}) \quad (8)$$

We also define:

$$\mathbf{W}(\mathbf{x}) = \text{diag}(W_i(\mathbf{x})) \quad (9)$$

We remark that the approximation is written in terms of the MLS “shape functions” $\mathbf{N}^T(\mathbf{x})$, that are depending on the grid. So, in fixed grids they will be computed only once.

The variables and its derivatives are computed by using these shape functions. Thus, in the FV-MLS method, the MLS approximation will be used to compute the derivatives needed for the reconstruction of variables at quadrature points at cell interfaces. We remember that the reconstruction step is made by using a Taylor expansion until m th order as presented in the previous section. The resulting scheme is a $(m + 1)$ th order method [26,24].

2.2.2. Kernel functions

The kernel function plays a key role in the properties of the scheme. Many functions may be used as kernels, as splines, Gaussians, exponentials. We refer the reader to the book of Liu [27] for more details. In the present work the 1D exponential kernel function is used. This kernel function is very well suited for anisotropic node distribution:

$$W(x_j - x_I, \kappa) = \frac{e^{-\left(\frac{s}{c}\right)^2} - e^{-\left(\frac{d_m}{c}\right)^2}}{1 - e^{-\left(\frac{d_m}{c}\right)^2}} \quad (10)$$

with $s = |x_j - x_I|$ with $j = 1, \dots, n_x$, $d_m = \max(|x - x_I|)$, $c = \frac{d_m}{2\kappa}$, x_I is the reference point (the point around which the stencil moves, in this case the centroid of each cell, I), and κ is a shape parameter. A 2D kernel is obtained by multiplying two 1D kernels. κ varies from 1 to 6 according to the applications. It is shown in [28,19] that the dispersion and dissipation characteristics of the FV-MLS method are strongly related to the choice of the κ parameter. For Euler and Navier–Stokes equations, a value of κ between 4 and 6 seems to be a good choice. It guarantees the good conditioning of the momentum matrix \mathbf{M} and an acceptable compromise of dispersion and dissipation.

2.3. Estimation of derivatives

2.3.1. Space derivatives

Moving Least-Squares Reproducing Kernel Approximations (MLS) presented in the previous section, is used to construct the high order continuous representation of $\mathbf{U}(\mathbf{x})$ and then its space derivatives.

It should be remembered that the general representation of $\mathbf{U}(\mathbf{x})$, which is approximated or reconstructed, is sought for in the subspace spanned by a set of basis functions $N(\mathbf{x})$ associated to the nodes, such that $\mathbf{U}(\mathbf{x})$ is a continuous function of the form:

$$\mathbf{U}(\mathbf{x}) = \sum_{j=1}^{n_x} N_j(\mathbf{x}) \mathbf{U}_j \quad (11)$$

Eq. (11) states that the approximation at a point \mathbf{x} in the vicinity of I , is computed using n_x surrounding nodes.

In a triangular unstructured grid, if we consider I the centroid of the active cell, then j are the centroids of the n_x surrounding cells. This leads to the construction of a stencil around I (see Fig. 1).

The number of cells in a stencil and their distribution around I will be discussed below.

Coming back to Eq. (1). Now all the derivatives can be computed using Eq. (11) as

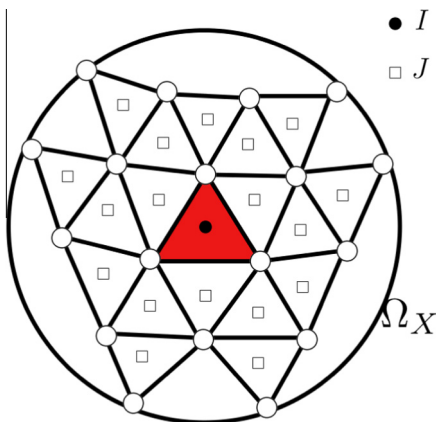


Fig. 1. Stencil support.

$$\frac{\partial^2 \mathbf{U}_I}{\partial x^{(\alpha-\beta)} \partial y^\beta} \approx \sum_{k=1}^{n_x} \frac{\partial^2 N_k(\mathbf{x}_I)}{\partial x^{(\alpha-\beta)} \partial y^\beta} \mathbf{U}_k \quad (12)$$

With $\alpha = 0$ to m and $\beta = 0$ to α , m being the derivative order.

It is important to notice that for a fixed grid (non-deforming grid), $N(\mathbf{x})$ and its derivatives are calculated just once at the beginning of computation. We also note that $N(\mathbf{x})$ is related to the grid topology.

2.3.2. Estimation of the shape function derivatives

According to Eq. (5) the shape function is given by,

$$N(\mathbf{x}) = \mathbf{p}^T \left(\frac{\mathbf{x} - \mathbf{x}_I}{h} \right) \mathbf{M}^{-1}(\mathbf{x}) \mathbf{P}_{\Omega_x} \mathbf{W}(\mathbf{x}) \quad (13)$$

Let's call,

$$\mathbf{C}(\mathbf{x}) = \mathbf{M}^{-1}(\mathbf{x}) \mathbf{P}_{\Omega_x} \mathbf{W}(\mathbf{x}) \quad (14)$$

such that,

$$N(\mathbf{x}) = \mathbf{p}^T \left(\frac{\mathbf{x} - \mathbf{x}_I}{h} \right) \mathbf{C}(\mathbf{x}) \quad (15)$$

Higher order derivative of $N(\mathbf{x}_I)$ at the centroid I is then given by:

$$\frac{\partial^2 N(\mathbf{x}_I)}{\partial x^{(\alpha-\beta)} \partial y^\beta} = \frac{\partial^2 p(\mathbf{0})}{\partial x^{(\alpha-\beta)} \partial y^\beta} \mathbf{C}(\mathbf{x}_I) + p(\mathbf{0}) \frac{\partial^2 \mathbf{C}(\mathbf{x}_I)}{\partial x^{(\alpha-\beta)} \partial y^\beta} \quad (16)$$

In Eq. (16), the derivation of the polynomial p is straightforward, contrary to the diffuse derivatives as derivatives higher than 2 are complicated to estimate analytically. This is why we assume that for $\alpha > 2$,

$$\frac{\partial^2 N(\mathbf{x}_I)}{\partial x^{(\alpha-\beta)} \partial y^\beta} \approx \frac{\partial^2 p(\mathbf{0})}{\partial x^{(\alpha-\beta)} \partial y^\beta} \mathbf{C}(\mathbf{x}_I) \quad (17)$$

The first and the second derivatives of \mathbf{C} are respectively,

$$\frac{\partial \mathbf{C}(\mathbf{x}_I)}{\partial x_i} = \mathbf{C}(\mathbf{x}_I) \mathbf{W}^{-1}(\mathbf{x}_I) \frac{\partial \mathbf{W}(\mathbf{x}_I)}{\partial x_i} (\mathbf{I} - \mathbf{P}_{\Omega_x}^T \mathbf{C}(\mathbf{x}_I)) \quad (18)$$

and

$$\begin{aligned} \frac{\partial^2 \mathbf{C}(\mathbf{x}_I)}{\partial x_i \partial x_j} &= \frac{\partial \mathbf{C}(\mathbf{x}_I)}{\partial x_j} \mathbf{W}^{-1}(\mathbf{x}_I) \frac{\partial \mathbf{W}(\mathbf{x}_I)}{\partial x_i} (\mathbf{I} - \mathbf{P}_{\Omega_x}^T \mathbf{C}(\mathbf{x}_I)) \\ &\quad - \mathbf{C}(\mathbf{x}_I) \frac{\partial \mathbf{W}(\mathbf{x}_I)}{\partial x_j} \mathbf{W}^{-2}(\mathbf{x}_I) \frac{\partial \mathbf{W}(\mathbf{x}_I)}{\partial x_i} (\mathbf{I} - \mathbf{P}_{\Omega_x}^T \mathbf{C}(\mathbf{x}_I)) \\ &\quad + \mathbf{C}(\mathbf{x}_I) \mathbf{W}^{-1}(\mathbf{x}_I) \frac{\partial^2 \mathbf{W}(\mathbf{x}_I)}{\partial x_i \partial x_j} (\mathbf{I} - \mathbf{P}_{\Omega_x}^T \mathbf{C}(\mathbf{x}_I)) \\ &\quad - \mathbf{C}(\mathbf{x}_I) \mathbf{W}^{-1}(\mathbf{x}_I) \frac{\partial \mathbf{W}(\mathbf{x}_I)}{\partial x_i} \mathbf{P}_{\Omega_x}^T \frac{\partial \mathbf{C}(\mathbf{x}_I)}{\partial x_j} \end{aligned} \quad (19)$$

The subscripts i and j take the values 1 and 2 corresponding to x and y directions respectively. More details about the procedure used in this paper can be found in [29,19].

2.3.3. Time-dependent term treatment

The system to be solved has the form

$$\frac{\partial \mathbf{U}_I}{\partial t} = \mathbf{R}(\mathbf{U}_R|_I) \quad (20)$$

it can be solved using explicit time schemes.

\mathbf{U}_I is considered as the mean value of the vector of variables \mathbf{U} at the active cell such as $\int_{V_I} \mathbf{U} dV \approx V \mathbf{U}_I$. A sine qua non condition to enforce the conservation of the mean consists of replacing the continuous reconstruction in the time-dependent term by the discontinuous one \mathbf{U}_R .

A manner to enforce the conservation of the mean is the use of zero-mean polynomials in the expansion (1). In this case Eq. (1) reads,

$$\begin{aligned} \mathbf{U}_R(\mathbf{x})|_I &= \mathbf{U}_I + (x - x_I) \frac{\partial \mathbf{U}_I}{\partial x} + (y - y_I) \frac{\partial \mathbf{U}_I}{\partial y} \\ &+ \sum_{\alpha=2}^m \sum_{\beta=0}^{\alpha} \frac{1}{\beta! (\alpha - \beta)!} \left[(x - x_I)^{(\alpha - \beta)} (y - y_I)^{\beta} - \Theta_{\alpha\beta} \right] \\ &\times \frac{\partial^{\alpha} \mathbf{U}_I}{\partial x^{(\alpha - \beta)} \partial y^{\beta}} + o(m) \end{aligned} \quad (21)$$

where, $\Theta_{\alpha\beta} = \frac{\varpi_{x^{(\alpha - \beta)} y^{\beta}}}{V_I}$ is the correction term ensuring the zero-mean, and $\varpi_{x^{\alpha} y^{\beta}} = \int_{V_I} (x - x_I)^{\alpha} (y - y_I)^{\beta} dV$ is estimated using a symmetric quadrature presented in [30] by Wandzura et al.

This reconstruction can be found in some mean-conservation restrictions used in other cell averaged finite volume method schemes, see [31,32] for instance. In our case, the mean-conservation correction appears a posteriori in the reconstruction contrary to the k-exact method for example, in which a priori mean-conservation restriction is imposed.

As described in [19], the use of zero-mean polynomials ensure at most a third space order of accuracy of the finite volume solver. The use of higher order MLS reconstruction (>3) will improve the accuracy but the overall space order of accuracy will always be limited to three. In what follows, when we will discuss about scheme accuracy aspects concerning the two phases model, the term “order of MLS reconstruction” will be used instead of “space order of accuracy”. The use of a full mass matrix formulation will overcome this limitation [19].

3. Two phases compressible flow

3.1. Conservation equations

The physical approach used in this study is based on the reduced five-equation model for two fluids, also named Kapila model [33]. As an important assumption, the pressure and the velocity vector at the two-phase interface are the same. In this context, there is a mass conservation equation for each phase. On the other hand, a unique conservation equation for the momentum and the energy is solved for both fluids. Furthermore, the volume fraction α is transported. This scalar defined between 0 and 1, is representing the amount of both fluids in the control volumes. For $\alpha = 0$, the cells are only occupied by the first fluid, whereas for $\alpha = 1$ the cells are only occupied by the second fluid. Finally, the system is given below for 2D flows:

$$\frac{\partial \mathbf{U}}{\partial t} + \frac{\partial \mathbf{F}(\mathbf{U})}{\partial x} + \frac{\partial \mathbf{G}(\mathbf{U})}{\partial y} = \mathbf{S} \quad (22)$$

$$\text{where } \mathbf{U} = \begin{pmatrix} \alpha \\ (1 - \alpha)\rho_1 \\ \alpha\rho_2 \\ \rho u \\ \rho v \\ \rho E \end{pmatrix}, \mathbf{F}(\mathbf{U}) = \begin{pmatrix} \alpha u \\ (1 - \alpha)\rho_1 u \\ \alpha\rho_2 u \\ \rho u^2 + p \\ \rho u v \\ (\rho E + p)u \end{pmatrix} \quad \text{and} \\ \mathbf{G}(\mathbf{U}) = \begin{pmatrix} \alpha v \\ (1 - \alpha)\rho_1 v \\ \alpha\rho_2 v \\ \rho u v \\ \rho v^2 + p \\ (\rho E + p)v \end{pmatrix}.$$

In the above system, ρ is the mixture density obtained from $\rho = (1 - \alpha)\rho_1 + \alpha\rho_2$, (u, v) are the velocity components, p is the static pressure, E is the total energy and \mathbf{S} is a source term including the external forces as well.

The transport of the volume fraction does not preserve the conservation for compressible flow. The advection equation can still be modified in a conservative form with an additional term as following [34]:

$$\frac{\partial \alpha}{\partial t} + u \frac{\partial \alpha}{\partial x} + v \frac{\partial \alpha}{\partial y} = \frac{\partial \alpha}{\partial t} + \frac{\partial(\alpha u)}{\partial x} + \frac{\partial(\alpha v)}{\partial y} - \alpha \left(\frac{\partial u}{\partial x} + \frac{\partial v}{\partial y} \right) \quad (23)$$

In this case, the volume fraction equation can be added to the left part of the system (22), whereas the last term $\alpha \nabla \cdot \mathbf{u}$ is included in the source term, $\mathbf{u} = (u, v)$ being the velocity vector.

3.2. Equations of state

The system introduced in the previous section is closed with the relevant equation of states for both fluids. Thereby, the stiffened gas equations of state is used to compute the physical properties of the fluids, namely the pressure, the sound speed and the temperature. The model presented here is a one pressure model, and the latter fluid properties are thus the properties of the mixture.

The three equations are presented below, where e stands for the internal energy such as $E = e + \frac{u^2 + v^2 + w^2}{2}$, γ stands for the heat capacity ratio, and π is a pressure reference that approximates a relative pressure-independence, which is usually used for liquids. In the case $\pi = 0$, the stiffened gas equation is equivalent to the perfect gas law. Finally, C_p stands for the heat capacity.

$$p = (\gamma - 1)\rho e - \gamma\pi \quad (24)$$

$$c^2 = \gamma \frac{p + \pi}{\rho} = (\gamma - 1)C_p T \quad (25)$$

$$T = \frac{p + \pi}{\rho C_p} \frac{\gamma}{\gamma - 1} \quad (26)$$

For the mixture cells where α is between 0 and 1, a mixture heat capacity ratio $\tilde{\gamma}$ and pressure reference $\tilde{\pi}$ are calculated in function of the volume fraction [35,34]. These formulations are given in Eqs. (27) and (28), where the subscript k denotes both phases. The introduced modification avoid a jump of the latter parameters across the interface.

$$\tilde{\gamma} = 1 + \frac{1}{\sum \frac{\alpha_k}{\gamma_k - 1}} \quad (27)$$

$$\tilde{\pi} = \frac{\sum \frac{\alpha_k \gamma_k \pi_k}{\gamma_k - 1}}{\left(1 + \sum \frac{\alpha_k}{\gamma_k - 1} \right)} \quad (28)$$

4. Boundedness preservation

From a physical point of view, the volume fraction has to be bounded between 0 and 1. However, the boundedness preservation of an advected scalar is not straightforward for high order schemes. The proposed method presented in this work is similar to the BQUICK scheme [36]. The proposed algorithm, described below, decreases locally the spatial order of accuracy to the first order which unconditionally ensures the boundedness. This modification is taken into account through the correction of the flux.

The algorithm is of a predictor-corrector type. An intermediary time step is performed initially in order to list the cells where the volume fraction is exceeding the bounds. Then, until convergence, the fluxes at each faces of these control volumes are re-computed without using the MLS reconstruction for the variable. Immediately afterward, a check is performed to get the new cells with an exceeding volume fraction. One considers that the convergence is reached when the list of the control volumes exceeding the bounds remain the same after a new flux computation. In the present algorithm, $\varphi_j(\alpha_i^{X,n})$ stands for the flux at the j th face of the i th cell for a variable α reconstructed with an order X , while

$R(\alpha_i^n)$ is the total residual of the considered variable for the considered control volume. This algorithm is explicit in time.

Algorithm 1. Algorithm for boundedness preservation of the two phases-MLS approach

```

for all control volumes  $\Omega_i$  do
     $\alpha_i^* = \alpha_i^n - \frac{\Delta t}{\Omega_i} R(\alpha_i^n)$ 
end for
while  $\tilde{c}t \neq ct$ 
     $\tilde{c}t = 0$ 
    for all control volumes  $\Omega_i$  do
        if  $(\alpha_i^* < 0)$  or  $(\alpha_i^* > 1)$  then
             $\tilde{c}t = \tilde{c}t + 1$ 
            for all faces  $F_j$  of  $\Omega_i$ 
                 $R(\alpha_i^n) = R(\alpha_i^n) - (\varphi_j(\alpha_i^{X,n}) - \varphi_j(\alpha_i^{1,n}))$ 
            end for
        end if
    end for
     $ct = 0$ 
    for all control volumes  $\Omega_i$  do
         $\alpha_i^* = \alpha_i^n - \frac{\Delta t}{\Omega_i} R(\alpha_i^n)$ 
        if  $(\alpha_i^* < 0)$  or  $(\alpha_i^* > 1)$  then
             $ct = ct + 1$ 
        end if
    end for
end while
for all control volumes  $\Omega_i$  do
     $\alpha_i^{n+1} = \alpha_i^n - \frac{\Delta t}{\Omega_i} R(\alpha_i^n)$ 
end for

```

This algorithm may also be used for the preservation of positiveness, as it could be important for the partial densities in the Kapila model [33,37] for instance. It is also important to note that the variables are exceeding their bounds only in some localized area, as illustrated by the computations in Fig. 2 (obtained for the test case in Section 5.2). Thereby, although the global space order of accuracy will be slightly reduced the overall error will remain low due to the high order MLS reconstruction.

5. Test cases

An explicit euler schemes is used for the time-discretization of our system of differential equation. The standard fluxes at cell faces are computed with the SLAU scheme, which stands for Simple Low-Dissipative AUSM (Advection Upstream Splitting Method)

[38]. This Riemann solver has good properties for high speed non-uniform flows.

5.1. Scalar transport

The criterion of low diffusivity and boundedness of our two phases model are validated with the stretching of a circle in a vortex velocity field [39,11]. This advection case allow to asses the capability of the high-order coupled two phases-MLS approach to correctly track the interface for strong deformations.

In this test case, only the volume fraction equation is solved. This variable is transported on a converged pressure and velocity field, without the source term introduced in Section 3.1 because of the relevant assumption of incompressibility for this test case.

The velocity field is described as following:

$$\begin{cases} u = -\sin(x)\cos(y) \\ v = -\cos(x)\sin(y) \end{cases} \quad (29)$$

The computational domain is a 2D square of length 1 m centered in (0,0). The resolution is performed with an unstructured mesh of around 150×150 triangle cells. Inside the domain, the scalar is initialized with a circle of radius 0.2 situated in (0,-0.25). Furthermore, the scalar concentration is defined by the following hyperbolic tangent function to ensure a relatively smooth interface: $\alpha(r) = 1 - (\frac{1}{2} + \frac{1}{2} \tanh(\frac{r-R}{a}))$. In our case, the slope a has been chosen equal to 0.01.

The time step is fixed to $\Delta t = 0.001$ s in order to respect at maximum a CFL of 0.25. After 2500 time iterations forward, the same number of time iterations is performed backward with the reversed velocity field. Thereby, the scalar should recover his initial position with an ideal transport model.

From a mathematical point of view, the interface location corresponds to the iso volume fraction of 0.5. The results concerning this interface position are visible in Fig. 3, for a forward and a backward transport with the two phases-MLS approach, and for the backward transport using the QUICK approach of ANSYS Fluent. These results show the ability of the two phases-MLS method to correctly recover the true interface after a strong deformation, without any reconstruction method. The correspondence of the transported interface and the initial one is as good as for the QUICK method. Furthermore, a higher MLS schemes leads obviously to a lower diffusivity of the scalar. However, a non-smooth interface is obtained with schemes above the 3rd order, and the spatial fluctuations of the interface are increasing with the order of the MLS method.

In order to perform a deeper analysis, the Table 1 underlines the efficiency of the different approaches. The results proves that all these methods have a good conservation property. Regarding the boundedness, the algorithm introduced in Section 4 avoid too important excess of the bounds for the proposed two phases-MLS

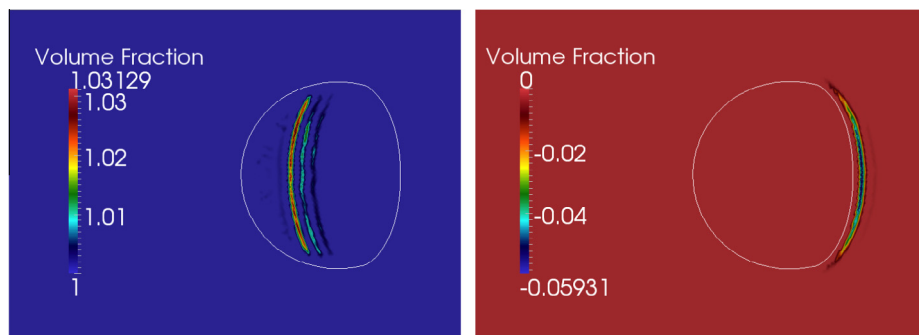


Fig. 2. Contours of exceeding volume fraction, above the upper bound (left) and below the lower bound (right). The interface ($\alpha = 0.5$) is represented by the white lines.

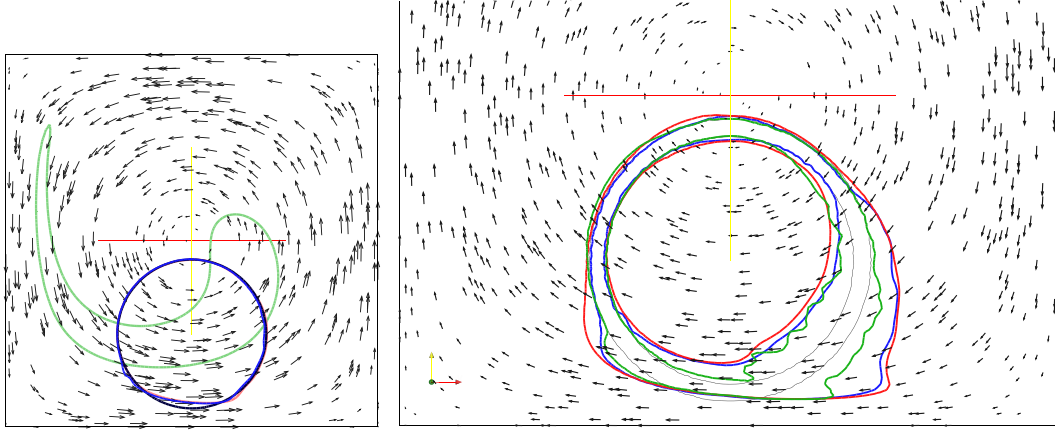


Fig. 3. (Left) Computed interfaces at initial time (black), after 2500 iterations forward (using a 3rd order MLS reconstruction in green), and after 2500 iterations forward and backward (using a 3rd order MLS reconstruction approach in red and the QUICK approach of Fluent in blue). (Right) Computed contours of volume fraction 0.1 and 0.9 at initial time (black), and after 2500 iterations forward and backward, using a 3rd order MLS reconstruction in red, a 4th order MLS reconstruction in green and the QUICK approach of Fluent in blue. Velocity field in background. (For interpretation of the references to colour in this figure legend, the reader is referred to the web version of this article.)

Table 1

Properties accuracy of the different numerical methods used for the scalar transport.

	MLS 3rd	MLS 4th	QUICK (Fluent)
Conservation	$<10^{-6}$	$<10^{-6}$	$\sim 10^{-6}$
Boundedness	$\sim 10^{-3}$	$\sim 10^{-4}$	$<10^{-6}$
Error E	0.132	0.0831	0.111

method. However, these excess are still two orders of magnitude larger with the 4th order reconstruction than with the QUICK approach. The general accuracy of the different methods are finally estimated with the error E , calculated as following:

$$E = \frac{\sum_i |\alpha_i^f - \alpha_i^0| \Omega_i}{\sum_i \alpha_i^0 \Omega_i} \quad (30)$$

In the previous equation, α^0 stands for the volume fraction at initial time, whereas α^f stands for the volume fraction after the 5000 iterations forward and backward. It appears thus that despite the development of a non-smooth interface, high order MLS methods lead to a better accuracy in comparison to the QUICK method of Fluent.

5.2. 2D interaction between shock and bubbles

The two following test cases aim to simulate the propagation of a shock respectively through a helium bubble, and a R22 bubble [34,40,41]). The pressure waves generated by the impact between the shock and the bubbles are expected to strongly deform these ones, and mix the air with the secondary gas. These experiments were originally performed by Haas & Sturtevant [42], inside a rectangular channel whose walls are reflecting the waves.

The computational domain is a 2D rectangular box of dimension $267 \times 89 \text{ mm}^2$, as described in Fig. 4. A bubble with a diameter of 50 mm is initially placed in the box. Furthermore, the air is present in two states at initial time, in a pre-shock state and in a post-shock state. The shock is going from the right to the left of the domain at 1.22 Mach velocity. The gas properties and initial conditions for the two test cases are listed in Table 2. As stated in Section 3.2, the equation of state used to compute the thermodynamics properties of the gases is the perfect gas law (stiffened gas law with a zero pressure reference).

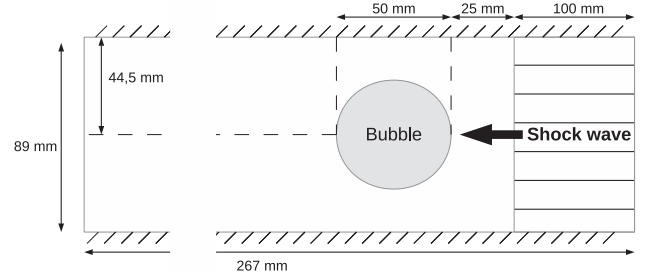


Fig. 4. Diagram of the computational domain and the initial condition of the air-bubble interaction.

Table 2

Gas properties and initial condition for the interaction between a shock wave and a helium bubble.

	γ	$\rho \text{ (kg m}^{-3}\text{)}$	$u \text{ (m s}^{-1}\text{)}$	$P \text{ (bar)}$
Pre-shock air	1.400	1.400	0.000	1.000
Post-shock air	1.400	1.927	-114.4	1.570
Helium	1.648	0.2546	0.000	1.000
R22	1.249	4.4154	0.000	1.000

For these test cases, the boundedness of the volume fraction is preserved as well, according to the Algorithm 1. In addition, the positiveness of both density $(1 - \alpha)\rho_1$ and $\alpha\rho_2$ are also ensured thanks to the algorithm.

The domain is meshed in 108,278 uniform triangular cells, with a base size of 0.7 mm. The results presented below are obtained with a 3rd MLS reconstruction approach. The grid is applied over the entire domain without using any symmetry condition. In this conditions, the symmetry of the density contour presented in Figs. 5 and 6 is not forced. It is a results of the computations.

5.2.1. Helium bubble

The numerical results are shown in Fig. 5 for the helium bubble, in parallel to the experimental results of Haas and Sturtevant [42]. The simulation results represent the contours of density, while the experimental results are shadow-photographs. The general physical behavior of the interaction between the shock and the helium bubble is well reproduced. A curved shaped reflected wave is

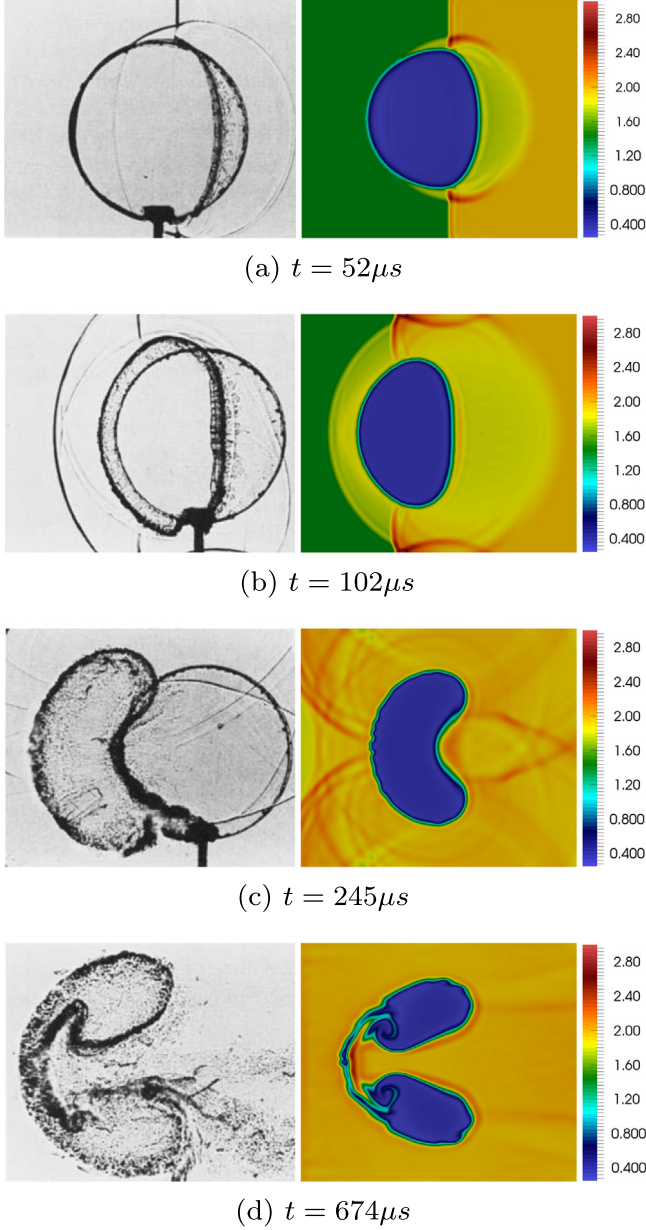


Fig. 5. Comparison between shadow-photographs [42] (left) and density contours from simulation (right).

already present at $t = 52 \mu s$ (Fig. 5a), due to the initial impact between the shock and the bubble. The interaction between this reflected wave and the incoming shock induces high densities, localized at the right of the junction between the incoming shock and the bubble. Because of the difference of speeds of sound, the transmitted wave which is propagating inside the helium bubble is finally ahead of the shock wave at $t = 102 \mu s$, as it is visible in Fig. 5b. Furthermore, once the transmitted wave has completely crossed the bubble, the latter starts to move with the flow. At time $t = 102 \mu s$, one can also see that the first reflected wave is again reflected by the tube walls (top and bottom of the figure). These second reflections form a complex ripple-like structure, visible at $t = 245 \mu s$ in Fig. 5c. During the following times, a jet of air is piercing the bubble. Because of the difference of densities between air and helium, a Kelvin–Helmholtz instability is generated, and the jet is thus rolling up inside the bubble in a clockwise direction, as it is shown in Fig. 5d.

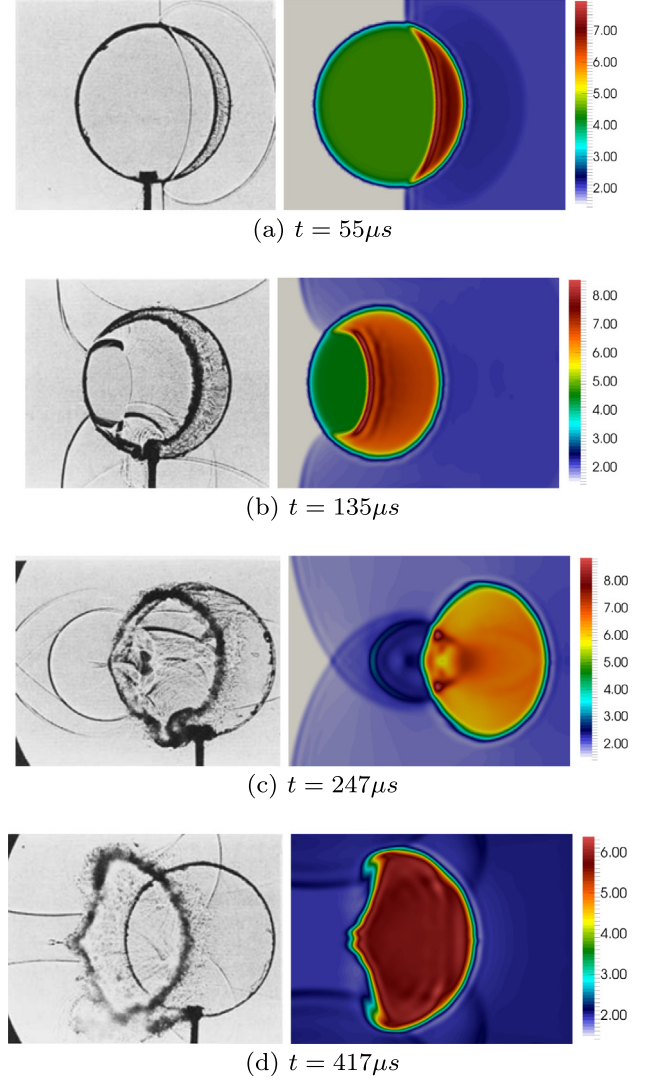


Fig. 6. Comparison between shadow-photographs [42] (left) and density contours from simulation (right).

5.2.2. R22 bubble

The numerical results are shown in Fig. 6 for the R22 bubble, in parallel to the experimental results of Haas and Sturtevant [42]. In Fig. 6a the incoming shock starts to compress the bubble. Notice also the reflected pressure wave on the right hand side of the bubble. The propagation of the shock inside the bubble is slower than in the surrounding air due to lower speed of sound in R22. In Fig. 6b the incoming shock become curved as it exit the bubble. In Fig. 6c, the upper and lower pressure waves focus inside the bubble creating a small zone of high density. In Fig. 6d, the shock has passed the bubble which has been strongly deformed. Notice the pressure waves reflected from the side wall and the curling vortices at the interface due to a Richtmyer–Meshkov instability. For the 4 instants presented in Fig. 6, the shapes of density contours are in very good agreement with the experimental shadow graphs.

5.2.3. Quantitative results

In order to show the accuracy of the proposed method, quantitative results of wave speed are presented for comparison in Table 3 for Helium bubble and in Table 4 for R22. The obtained results are in the same range of accuracy of both experiments of

Table 3

Comparison of available results of speeds, in m/s, of incoming shock, c_{is} , refracted shock, c_{rs} , and right side of interface, c_{ui} , as found in helium bubble experiment [42].

	c_{is}	c_{rs}	c_{ui}
Experiments from Haas [42]	410	900	170
Computations of Quirk [43]	422	943	178
Computations of Kreeft [33]	419	956	176
Present work, fine mesh	427	948	184
Present work, coarse mesh	409	949	185

Table 4

Comparison of available results of speeds, in m/s, of incoming shock, c_{is} , refracted shock, c_{rs} , and right side of interface, c_{ui} , as found in R22 bubble experiment [42].

	c_{is}	c_{rs}	c_{ui}
Experiments from Haas [42]	415	240	73
Computations of Quirk [43]	420	254	70
Computations of Kreeft [33]	419	241	75
Present work, fine mesh	422	234	68
Present work, coarse mesh	413	231	69

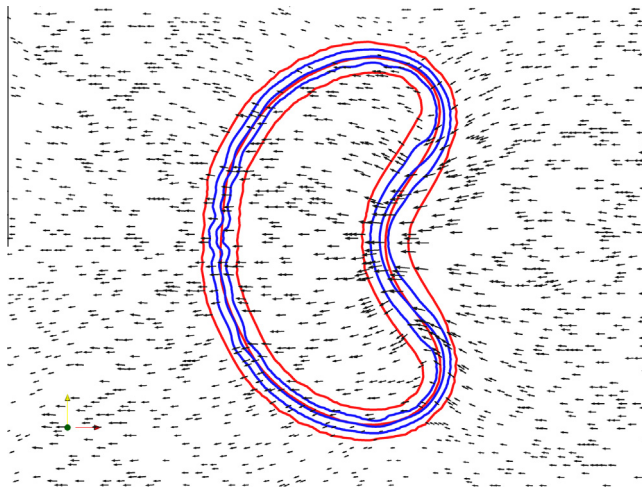


Fig. 7. Computed contours of helium bubble volume fraction $\alpha = 0.1$, $\alpha = 0.5$ and $\alpha = 0.9$, on a coarse (in blue) and on a fine mesh (in red). Velocity field in background. (For interpretation of the references to colour in this figure legend, the reader is referred to the web version of this article.)

Haas and Sturtevant [42] in one hand and numerical simulations of Kreeft and Koren [33] and Quirk and Karni [43] in the other hand, although the mesh quality used in this paper is really lower. Indeed, Quirk and Karni [43] used a quadrangle meshes with two levels of local refinement, which is equivalent to 12,800,000 cells according to the authors, whereas Kreeft and Koren [33] used a uniform structured meshes of 320,000 cells with a symmetry condition. In this study, computation were carried out on two different meshes: fine mesh and coarse mesh. The fine mesh has 108,278 triangular cells, whereas the coarse one has only 13,664 triangular cells (base size of 2 mm). Results for both meshes are in good agreement with the literature.

From the results presented in Tables 3 and 4, it appears clearly that the use of a coarse mesh with our method is sufficient to obtain satisfactory quantitative results.

Similarly, a high order FV-MLS approach is able to catch correctly the bubble deformation and compression along the time. With a sufficiently fine mesh, this method reproduces the small fluctuation of the left interface of the helium bubble, and calculates as well the vortices of the Kelvin–Helmholtz instability without any reconstruction method. This subject is illustrated by the Fig. 7, where the contours of volume fraction are plotted for two

meshes of different level of refinement. The volume fraction diffusion obtained with the coarse mesh remains reasonable. In addition, the interface position is very similar for both meshes.

These results underline the capability of the high order FV-MLS approach to correctly simulate two components flows, even on coarse meshes, similarly to the methods based on interface reconstruction.

6. Conclusion

A compressible two-phase Kapila model using a high order finite volume solver has been presented in this paper. In the context of solving two-phase flow problems, the critical point is to combine mass conservation and high accuracy, with a boundedness preservation. While the mass conservation is inherent to the two-phase model, the high accuracy is provided here by a finite volume solver using moving least squares reconstruction developed for unstructured mesh. In order to compensate the unboundedness induced by high order accuracy schemes, a simple algorithm is proposed. The global approach is thus naturally anti-diffusive, without any artificers for interface reconstruction. The latter allows for the meshing stage of the problem to be simplified, by using more or less coarse and unstructured grid (sometimes essential for very complex geometries), and avoiding a significant loss of accuracy. Our method is firstly examined by its ability to analyze strong deformations of the interface. The present results showed a similar efficiency than commercial code with interface reconstruction. The second and third test cases demonstrated that the FV-MLS method can also handle complex compressible flows, with satisfactory results. In addition, the structure of this approach also makes it easily applicable to incompressible flows.

References

- [1] Hirt C, Nichols B. Volume of fluid (VOF) method for the dynamics of free boundaries. *J Comput Phys* 1981;39(1):201–25. [http://dx.doi.org/10.1016/0021-9991\(81\)90145-5](http://dx.doi.org/10.1016/0021-9991(81)90145-5). <<http://linkinghub.elsevier.com/retrieve/pii/S0021999181901455>>.
- [2] Noh W, Woodward P. SLIC (simple line interface calculation). In: Vooren A, Zandbergen P, editors. Proceedings of the fifth international conference on numerical methods in fluid dynamics June 28 – July 2, 1976 Twente University, Enschede. Lect notes phys, vol. 59. Berlin, Heidelberg: Springer; 1976. p. 330–40. http://dx.doi.org/10.1007/3-540-08004-X_336.
- [3] Youngs D. Time-dependent multi-material flow with large fluid distortion. *Numer Methods Fluid Dyn* 1982;24:273–85.
- [4] Aulisa E, Manservigi S, Scardovelli R, Zaleski S. Interface reconstruction with least-squares fit and split advection in three-dimensional Cartesian geometry. *J Comput Phys* 2007;225(2):2301–19. <http://dx.doi.org/10.1016/j.jcp.2007.03.015>. <<http://linkinghub.elsevier.com/retrieve/pii/S0021999107001325>>.
- [5] Albadawi a, Donoghue D, Robinson a, Murray D, Delauré Y. Influence of surface tension implementation in volume of fluid and coupled volume of fluid with level set methods for bubble growth and detachment. *Int J Multiph Flow* 2013;53:11–28. <http://dx.doi.org/10.1016/j.ijmultiphaseflow.2013.01.005>. <<http://linkinghub.elsevier.com/retrieve/pii/S0301932213000190>>.
- [6] Ubbink O, Issa R. A method for capturing sharp fluid interfaces on arbitrary meshes. *J Comput Phys* 1999;153(1):26–50. <http://dx.doi.org/10.1006/jcph.1999.6276>. <<http://linkinghub.elsevier.com/retrieve/pii/S0021999199962769>>.
- [7] Chen Y, Price W, Temarel P. An anti-diffusive volume of fluid method for interfacial fluid flows. *Int J Numer Methods Fluids* 2012(January 2011): 341–59. <http://dx.doi.org/10.1002/flid>. <<http://onlinelibrary.wiley.com/doi/10.1002/flid.2509/full>>.
- [8] Sambasivan SK, UdayKumar H. Sharp interface simulations with local mesh refinement for multi-material dynamics in strongly shocked flows. *Comput Fluids* 2010;39(9):1456–79. <http://dx.doi.org/10.1016/j.compfluid.2010.04.014>. <<http://linkinghub.elsevier.com/retrieve/pii/S0045793010001052>>.
- [9] Sussman M, Smereka P, Osher S. A level set approach for computing solutions to incompressible two-phase flow. *J Comput Phys*. <<http://www.sciencedirect.com/science/article/pii/S0021999184711557>>.
- [10] Sussman M, Puckett EG. A coupled level set and volume-of-fluid method for computing 3D and axisymmetric incompressible two-phase flows. *J Comput Phys* 2000;162(2):301–37. <http://dx.doi.org/10.1006/jcph.2000.6537>. <<http://linkinghub.elsevier.com/retrieve/pii/S0021999100965379>>.
- [11] Lv X, Zou Q, Zhao Y, Reeve D. A novel coupled level set and volume of fluid method for sharp interface capturing on 3D tetrahedral grids. *J Comput Phys*

- 2010;229(7):2573–604. <http://dx.doi.org/10.1016/j.jcp.2009.12.005>. <<http://linkinghub.elsevier.com/retrieve/pii/S0021999109006767>>.
- [12] Yang X, James AJ, Lowengrub J, Zheng X, Cristini V. An adaptive coupled level-set/volume-of-fluid interface capturing method for unstructured triangular grids. *J Comput Phys* 2006;217(2):364–94. <http://dx.doi.org/10.1016/j.jcp.2006.01.007>. <<http://linkinghub.elsevier.com/retrieve/pii/S0021999106000143>>.
 - [13] Baer MR, Nunziato JW. A two-phase mixture theory for the deflagration-to-detonation transition (ddt) in reactive granular materials. *Int J Multiph Flow* 1986;12(6):861–89.
 - [14] Kapila aK, Son SF, Bdzil JB, Menikoff R, Stewart DS. Two-phase modeling of DDT: structure of the velocity-relaxation zone. *Phys Fluids* 1997;9:3885. <http://dx.doi.org/10.1063/1.869488>. <<http://link.aip.org/link/PHFLE6/v9/i12/p3885/s1&Agg=doi>>.
 - [15] Saurel R, Cocchi J, Butler P. A numerical study of cavitation in the wake of a hypervelocity underwater profile. *J Propul Power* 1999;15(4):513–22.
 - [16] Ambroso a, Chalons C, Raviart P-a. A Godunov-type method for the seven-equation model of compressible two-phase flow. *Comput Fluids* 2012;54:67–91. <http://dx.doi.org/10.1016/j.compfluid.2011.10.004>. <<http://linkinghub.elsevier.com/retrieve/pii/S0045793011003033>>.
 - [17] Yeom G-S, Chang K-S. A modified HLLC-type Riemann solver for the compressible six-equation two-fluid model. *Comput Fluids* 2013;76:86–104. <http://dx.doi.org/10.1016/j.compfluid.2013.01.021>. <<http://linkinghub.elsevier.com/retrieve/pii/S0045793013000455>>.
 - [18] Tian B, Toro E, Castro C. A path-conservative method for a five-equation model of two-phase flow with an HLLC-type Riemann solver. *Comput Fluids* 2011;46(1):122–32. <http://dx.doi.org/10.1016/j.compfluid.2011.01.038>. <<http://linkinghub.elsevier.com/retrieve/pii/S0045793011000454>>.
 - [19] Khelladi S, Nogueira X, Bakir F, Colominas I. Toward a higher order unsteady finite volume solver based on reproducing kernel methods. *Comput Methods Appl Mech Eng* 2011;200(29–32):2348–62. <http://dx.doi.org/10.1016/j.cma.2011.04.001>. <<http://www.sciencedirect.com/science/article/pii/S0045782511001344>>.
 - [20] Waterson N, Deconinck H. Design principles for bounded higher-order convection schemes – a unified approach. *J Comput Phys* 2007;224(1):182–207. <http://dx.doi.org/10.1016/j.jcp.2007.01.021>. <<http://linkinghub.elsevier.com/retrieve/pii/S002199910700040X>>.
 - [21] Vincent P, Caltagirone J.-p. Efficient solving method for unsteady incompressible interfacial flow problems 811 (September 1997); 1999: p. 795–811.
 - [22] Jasak H, Weller H, Gosman A. High resolution NVD differencing scheme for arbitrarily unstructured meshes. *Int J Numer Methods Fluids* 1999;449(July 1998):431–49. <<http://powerlab.fsb.hr/ped/kturbo/Openfoam/papers/GammaPaper.pdf>>.
 - [23] Lancaster P, Salkauskas K. Surfaces generated by moving least squares. *Math Comput* 1981;155:141–58.
 - [24] Cueto-Felgueroso L, Colominas I, Nogueira X, Navarrina F, Casteleiro M. Finite volume solvers and moving least-squares approximations for the compressible Navier–Stokes equations on unstructured grids. *Comput Methods Appl Mech Eng* 2007;196:4712–36.
 - [25] Liu WK, Hao W, Chen Y, Jun S, Gosz J. Multi-resolution reproducing kernel particle methods. *Comput Mech* 1997;20:295–309.
 - [26] Cueto-Felgueroso L, Colominas I, Fe J, Navarrina F, Casteleiro M. High-order finite volume schemes on unstructured grids using moving least squares reconstruction. Application to shallow water dynamics. *Int J Numer Methods Eng* 2006;65(3):295–331.
 - [27] Liu GR. Mesh free methods: moving beyond the finite element method. Boca Raton: CRC Press; 2003.
 - [28] Nogueira X, Colominas I, Cueto-Felgueroso L, Khelladi S. On the simulation of wave propagation with a higher-order finite volume scheme based on reproducing kernel methods. *Comput Methods Appl Mech Eng* 2010;199(23–24):1471–90.
 - [29] Nogueira X. Moving least squares and high-order finite volume methods for the numerical simulation of compressible flows (in spanish) [Ph.D. thesis]/ Universidade da Coruña; 2009.
 - [30] Wandzura S, Xiao H. Symmetric quadrature rules on a triangle. *Comput Math Appl* 2003;45:1829–40.
 - [31] Barth T, Frederickson P. Higher-order solution of the Euler equations on unstructured grids using quadratic reconstruction. In: AIAA paper 90-0013; 1990.
 - [32] Ollivier-Gooch C, Nejat A, Michalak K. On obtaining high-order finite-volume solutions to the Euler equations on unstructured meshes. In: AIAA paper 2007-4464, 18th AIAA computational fluid dynamics conference, Miami, FL, 25–28 June 2007.
 - [33] Kreeft JJ, Koren B. A new formulation of Kapila's five-equation model for compressible two-fluid flow, and its numerical treatment. *J Comput Phys* 2010;229(18):6220–42. <http://dx.doi.org/10.1016/j.jcp.2010.04.025>. <<http://linkinghub.elsevier.com/retrieve/pii/S0021999110002019>>.
 - [34] Ansari M, Daramizadeh S. Numerical simulation of compressible two-phase flow using a diffuse interface method. *Int J Heat Fluid Flow* 2013;42:209–23. <http://dx.doi.org/10.1016/j.ijheatfluidflow.2013.02.003>. <<http://linkinghub.elsevier.com/retrieve/pii/S0142727X13000386>>.
 - [35] Shyue K. A volume-of-fluid type algorithm for compressible two-phase flows. Hyperbolic problems: theory, numerics, applications (1). <http://link.springer.com/chapter/10.1007/978-3-0348-8724-3_40>.
 - [36] Herrmann M, Blanquart G, Raman V. Flux corrected finite volume scheme for preserving scalar boundedness in reacting large-eddy simulations. *AIAA J* 2006;44(12):2879–86. <http://dx.doi.org/10.2514/1.18235>.
 - [37] Schwendeman D, Wahle C, Kapila A. The Riemann problem and a high-resolution Godunov method for a model of compressible two-phase flow. *J Comput Phys* 2006;212(2):490–526. <http://dx.doi.org/10.1016/j.jcp.2005.07.012>. <<http://linkinghub.elsevier.com/retrieve/pii/S002199910500330X>>.
 - [38] Shima E, Kitamura K. On new simple low-dissipation scheme of AUSM-family for all speeds. AIAA Paper; 2009: (January). p. 1–15. <<http://arc.aiaa.org/doi/pdf/10.2514/6.2009-136>>.
 - [39] Gerlach D, Tomar G, Biswas G, Durst F. Comparison of volume-of-fluid methods for surface tension-dominant two-phase flows. *Int J Heat Mass Transfer* 2006;49:740–54. <http://dx.doi.org/10.1016/j.ijheatmasstransfer.2005.07.045>. <<http://www.sciencedirect.com/science/article/pii/S0017931005005314>>.
 - [40] Qamar S, Ahmed M. A high order kinetic flux-vector splitting method for the reduced five-equation model of compressible two-fluid flows. *J Comput Phys* 2009;228(24):9059–78. <http://dx.doi.org/10.1016/j.jcp.2009.09.010>. <<http://linkinghub.elsevier.com/retrieve/pii/S0021999109004951>>.
 - [41] Terashima H, Tryggvason G. A front-tracking/ghost-fluid method for fluid interfaces in compressible flows. *J Comput Phys* 2009;228(11):4012–37. <http://dx.doi.org/10.1016/j.jcp.2009.02.023>. <<http://linkinghub.elsevier.com/retrieve/pii/S0021999109000898>>.
 - [42] Haas J-F, Sturtevant B. Interaction of weak shock waves with cylindrical and spherical gas inhomogeneities. *J Fluid Mech* 2006;181(–1):41. <http://dx.doi.org/10.1017/S0022112087002003>. <http://www.journals.cambridge.org/abstract_S0022112087002003>.
 - [43] Quirk J, Karni S. On the dynamics of a shock-bubble interaction. *J Fluid Mech* 1996;318:129–63. <<http://www.sciencedirect.com/science/article/pii/S0262885606001788>> <http://journals.cambridge.org/abstract_S0022112096007069>.